Optics Letters

Multilayer deformation planarization by substrate pit suturing

Yingjie Chai,[1,2] Meiping Zhu,[1,*] Huanbin Xing,[1,2] Hu Wang,[1,2] Yun Cui,[1] and Jianda Shao[1,*]

[1]Key Laboratory of Materials for High Power Laser, Shanghai Institute of Optics and Fine Mechanics, Chinese Academy of Sciences, Shanghai 201800, China
[2]University of Chinese Academy of Sciences, No. 19 A, Yuquan Rd., Shijingshan District, Beijing 100049, China
*Corresponding author: bree@siom.ac.cn, jdshao@siom.ac.cn

Received 13 May 2016; revised 23 June 2016; accepted 27 June 2016; posted 27 June 2016 (Doc. ID 265154); published 18 July 2016

In the pursuit of 1064 nm high-power laser resistance dielectric coatings in the nanosecond region, a group of HfO_2/SiO_2 high reflectors with and without suture layers were prepared on prearranged fused silica substrates with femtosecond laser pits. Surface morphology, global coating stress, and high-resolution cross sections were characterized to determine the effects of substrate pit suturing. Laser-induced damage resistance was investigated for samples with and without suture layers. Our results indicate considerable stability in terms of the nanosecond 1064 nm laser-induced damage threshold for samples having a suture layer, due to decreased electronic field (e-field) deformation with simultaneous elimination of internal cracks. In addition, a suture layer formed by plasma ion-assisted deposition could effectively improve global mechanical stress of the coatings. By effectively reducing the multilayer deformation using a suture layer, electron-beam high-reflective coatings, whose laser-induced damage resistance was not influenced by the substrate pit, can be prepared.

OCIS codes: (140.3330) Laser damage; (230.4040) Mirrors; (240.0310) Thin films; (310.1860) Deposition and fabrication.

http://dx.doi.org/10.1364/OL.41.003403

Optical dielectric coatings have always played a significant role in high-power laser systems. With good optical quality and a relatively higher laser-induced damage threshold (LIDT), HfO_2/SiO_2 multilayer coatings prepared by electron-beam (EB) evaporation were the first choice for the 1ω laser facilities such as the National Ignition Facility (NIF) [1], Megajoule [2], and Shenguang [3]. Pulsed laser-induced damage to optical thin film coatings in the nanosecond (ns) region has been the object of continuous study in recent years [4]. For 1ω laser facility optics, one of the major limitations in preparing high LIDT coatings is substrate structural defects, such as contamination, particles, scratches, and pits [5–8]. For a rotating substrate in an EB evaporation coater, the multilayer dielectric coating growth exhibits a self-shadowing nature. Nodules originated from contamination and particle defects can be readily apparent on a given surface [8–10], but pit and scratch defects are typically buried under the coating layers and cannot be easily observed [11–13], especially on large-scale samples or hydrofluoric acid-etched substrate before deposition. Nodule defects could be recovered by a planarization coating process, utilizing the defect-smoothing technology principles originally developed for extreme ultraviolet lithography masks [14]. By a discrete process of angle-dependent ion etching and unidirectional ion-beam deposition, the planarization effect has been shown to increase the laser resistance of 1ω mirror coatings above 100 $J \cdot cm^{-2}$. Substrate scratches and pits are also considered a primary damage source and have attracted the most research attention in recent years [11–13]. However, scratches and pits cannot be effectively eliminated by current planarization technologies.

In this Letter, we focus primarily on substrate pit suturing during EB deposition. By depositing a suture layer between the substrate and a functional coating, pit defects could be effectively isolated. The LIDT of the coating on the prearranged substrate pits could be improved because of decreased deformation in the functional layers.

All the experiments were conducted on the same group of fused silica substrates that were 50 mm in diameter and 5 mm thick. We take a three-stage approach for the sample preparation, as listed in Table 1 and shown in Fig. 1. First, by using the fabrication method described in Refs. [15,16], different-sized pits were fabricated by 520 nm femtosecond laser pulses on a substrate of samples A-1 and A-2, respectively. The pit size was precisely controlled by femtosecond laser energy deposition. As measured by an atomic force microscope (AFM), the prepared pit diameters (depths) were 2.6 μm (280 nm), 3.6 μm (350 nm), 4.2 μm (420 nm), 4.7 μm (490 nm), 5.0 μm (510 nm), 5.2 μm (540 nm), and 6.0 μm (640 nm), respectively. Second, the A-2 substrate was coated by a 4680 nm single layer of SiO_2 as the suture layer by plasma ion-assisted deposition (PIAD) (voltage bias = 150 V) technology with an evaporation rate of 0.6 $nm \cdot s^{-1}$ and a starting pressure of 9×10^{-4} mbar. Substrates without pits (B-1 and B-3) were deposited by the same coating process as references. Third, high-reflective (HR) coatings with a coating stack of $Sub/4L(HL)^{12}H4L/A$ were prepared. Here, "Sub" denotes

Table 1. Sample Coating Stack and Substrate Arrangements

Sample	Stack Formula[a]	Substrate
A-1	$4L(HL)^{12}H4L$	With pit
A-2	$S4L(HL)^{12}H4L$	With pit
B-1	$S4L(HL)^{12}H4L$	Without pit
B-2	$4L(HL)^{12}H4L$	Without pit
B-3	S	Without pit

[a]"H" denotes HfO_2, "L" denotes SiO_2, and "S" denotes the 4680 nm suture layer. The substrate is to the left of the first layer, and the air is to the right of the last layer.

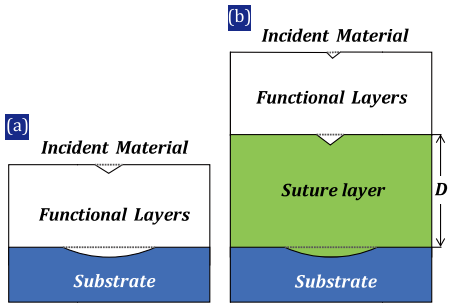

Fig. 1. Schematic introduction of samples (a) without and (b) with suture layer. The gray dashed lines denote the sample without pit (B-1 and B-2) and the solid outlines denote the sample with pit (A-1 and A-2). The incident medium was air, and the suture layer was a PIAD SiO_2 layer. The thickness of the suture layer was $D = 4,680$ nm.

the substrate and "H" and "L" denote HfO_2 and SiO_2, respectively. Both H and L had a quarter-wave optical thickness at a reference wavelength of 1064 nm (H:138 nm, L:183 nm). The coatings were deposited using Hf and SiO_2 as the starting materials. The ambient pressure for both HfO_2 and SiO_2 deposition was 2×10^{-2} Pa. SiO_2 was deposited at a rate of $\sim 0.3\ \text{nm} \cdot \text{s}^{-1}$, and HfO_2 was deposited at a lower rate of $\sim 0.09\ \text{nm} \cdot \text{s}^{-1}$. The refractive indices of HfO_2 and SiO_2 at 1064 nm are 1.912 and 1.449, respectively. The total physical thickness of the functional coatings was 5440 nm. In addition, sample B-2, having neither pits nor a suture layer, was evaporated with HR coatings in the same coating chamber as a reference The transmissions of the A-1, A-2, B-1, and B-2 samples (0°), which were lower than 0.5% at 1064 nm, were measured by a spectrometer (Lambda 1050 UV/VIS/NIR, Perkin-Elmer) with a transmittance measurement error of less than 0.08%.

The surface morphologies before and after HR coating deposition were investigated by AFM, and the coating surface roughness values with/without (B-2/B-1) a suture layer were 2.891 nm and 2.837 nm, respectively. Considering the uncertainty in the RMS calculations, the difference between the obtained surface roughness values is negligible. The suture layer with PIAD scarcely influences the surface roughness of the functional coatings in both the transverse and vertical directions. As shown in Fig. 2, the uncoated pit on substrate, coated pit without suture layer, and coated pit with suture layer, are shown in left-to-right order. The deformation in the functional layer was effectively relieved and the surface pits were closed or nearly closed. The effect of suturing had a direct correlation with the pit size and depth.

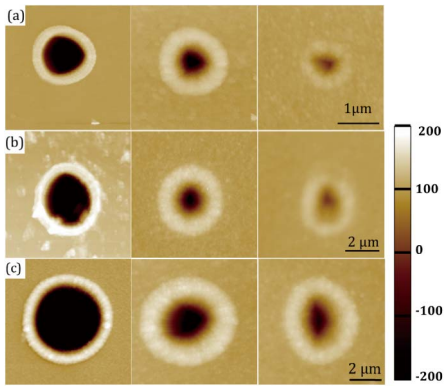

Fig. 2. (From left to right of each figure) AFM morphologies of uncoated substrate pit, coated pit without suture layer (sample A-1), and coated pit with suture layer (A-2) on sample of pit width of (a) 2.6 μm, (b) 4.2 μm, and (c) 6.0 μm.

None of these samples showed cracking failure during and after deposition. The surface shapes of our samples were characterized, because thick EB coatings may have mechanical shortcomings. The global mechanical properties of the reference samples B-1, B-2, and B-3 were characterized by a ZYGO Mark III-GPI interferometer at 632.8 nm. All tests were conducted at a relative humidity of 45 ± 5% and temperature of 22 ± 2°C. Substrate radii before (R1) and after (R2) deposition were used to calculate their coating stress (σ_{coatings}) utilizing Stoney's equation [17,18]:

$$\sigma_{\text{coatings}} = \frac{E_s}{6(1-\nu_s)} \cdot \frac{t_s^2}{t_f} \cdot \left(\frac{1}{R_2} - \frac{1}{R_1}\right), \tag{1}$$

$$f_{\text{total}} = \sigma_{\text{coatings}} \times \tau_{\text{layer}}. \tag{2}$$

Here, E_s and ν_s denote the Young's modulus and Poisson ratio of the substrate, respectively, while t_s and t_f represent the thicknesses of the substrate and the film, respectively. $E_s/(1-\nu_s)$ is the biaxial modulus of the film, which is equal to 86 GPa. Because the interface stress in our experiment was too weak and could be ignored, the total force (f_{total}) of the coatings can be defined using Eq. (2); the subsequent calculation results are shown in Table 2. The surface shapes of reference samples and the fused silica substrate were characterized by an interferometer, as shown in Fig. 3. The PIAD suture layer in sample B-3, which has a small pore size, has a packing density close to unity, leading to favorable compressive stress [17]. Samples B-1 and B-2 showed the same optical properties but opposite mechanical stresses; here, the suture layer transforms the functional layer surface shape from tension [Fig. 3(a3)] to compression [Fig. 3(a2)]. With a relatively high preloaded compressive stress, all coatings could endure a total coating thickness of 10.2 μm with no apparent coating cracking failure.

Table 2. Global Stress of the Samples[a]

Sample	B-1	B-2	B-3
σ_{coatings}(MPa)	−51.9	62.7	−200.4
f_{total}($\times 10^{-5}$ N/m)	−52.5	34.1	−93.8

[a]Negative values are compressive stress, while positive values are tensile stress. The statistical error of coating stress is less than 8%.

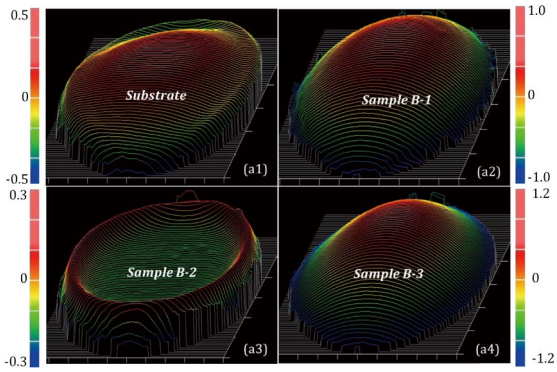

Fig. 3. Surface shape of (a1) substrate, (a2) B-1, (a3) B-2, and (a4) B-3. The color scale was on the unit of wavelength of $\lambda = 632.8$ nm.

As shown in Fig. 4, the scanning electron microscopy-focused ion beam (SEM-FIB) results demonstrated that one of the advantages of a suture layer is the decreased internal crack density caused by multilayer deformation. We have previously investigated the negative impacts of the internal cracks on laser resistance in Ref. [13]. The substrate pit deformational effects during deposition could be isolated by a suture layer. Due to the fast planetary rotation of the substrate during EB deposition, the difference in the deposition dynamic effects on the pits with greater breadth-depth ratios can be ignored. HfO_2 and SiO_2 multilayer growth could be considered synchronous perpendicular to both the substrate surface and pit sites. The pit was effectively flattened and the functional layer remained continuously geometrical in the transverse direction.

The LIDT was adapted from ISO standard 21254 and introduced in Refs. [19–21]. The 1-on-1 mode was used to evaluate the laser resistance of the entire sample, and raster scanning aimed at the pitted site was carried out to determine the laser resistance of the artificial defect itself. The laser damage system

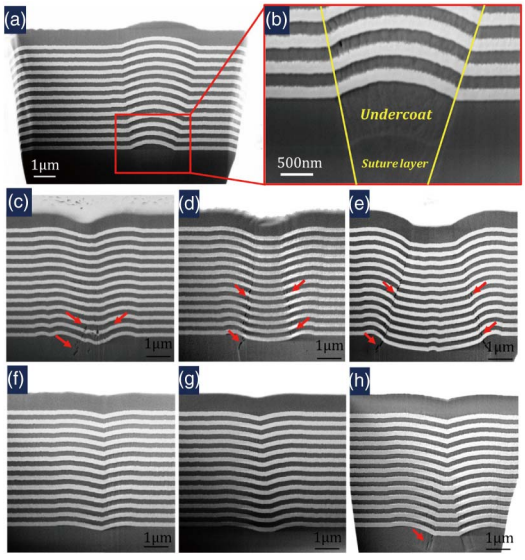

Fig. 4. (a) and (b) Cross section of nodule defect in B-1, originating from the suture layers. Cross section of A-1 with coated pit sizes of (c) 2.6 μm, (d) 4.2 μm, and (e) 6.0 μm. Cross section of A-2 above sutured layer with pit sizes of (f) 2.6 μm, (g) 4.2 μm, and (h) 6.0 μm. The red arrows indicate the internal crack in the coatings.

utilized in this work has been described in detail elsewhere [19,20]. Laser damage experiments were carried out using a 12 ns pulse from a 1064 nm Nd:YAG laser at a normal incidence angle. The e^{-2} spot diameters along the x and y axes were both 416 μm [22]. Damage was judged by comparison of the test area before and after laser irradiation on-line by a CCD detector. For 1-on-1 laser damage testing, 20 sites for each energy density were examined, and the morphologies of the damaged site were recorded. LIDT was defined as energy fluence of the incident pulse when the damage probability was 0%. The raster scanning aimed at the pitted site was halted either when more than 10 pits were damaged, or when catastrophic damage occurred [21]. The laser energy originated from a specific fluence that was based on previous 1-on-1 experiments, and gradually increased to the stop fluence by steps of 5–7 $J \cdot cm^{-2}$. The raster scanning region (10 mm × 10 mm) of B-1 and B-2 was examined to ensure that no visible structural defects existed before laser irradiation, for ruling out their influence on laser-resistance of the undeformed coatings.

The 1-on-1 LIDT of samples B-1 and B-2 were 64 $J \cdot cm^{-2}$ and 85 $J \cdot cm^{-2}$, respectively. The reduction of the laser resistance threshold for HR coatings with a suture layer was caused primarily by the larger coating thickness, which increased the risk of structure defect formation, like nodules. In fact, more nodule ejection damage was noticed on B-1 after 1-on-1 mode laser damage testing based on SEM-FIB observation. Based on FIB observations, the nodule defects originated mostly from the suture layer, as shown in Fig. 4(a), and led to the failure of the coating at lower laser fluence. For the pitted sample A-1, the 1-on-1 laser-induced damage probability was strongly influenced by both the pit size and the suture layer. However, A-2 had a relatively stable LIDT. The pit site was not damaged, and nodule ejection was the real bottleneck for improving the LIDT. In the raster scanning mode, the impact of pit size on the laser resistance of coatings with a suture layer was higher than for coatings without a suture layer, as shown in Fig. 5. The laser damage resistance was reduced as the pit size increased. Because the raster scanning mode was utilized and aimed at the pitted area, the damage results reflected the laser resistance of the pitted coating while ruling out the influence of nodule ejection. Unfortunately, the coating without a suture layer was seriously influenced in this regard by the substrate pits' size. The laser resistance of the HR coatings on pits could go as high as the LIDT of the undeformational coating at a pit width of 2.6 μm, and reach a lowest value of ~20 $J \cdot cm^{-2}$ at a pit width of 5.2 μm. The damage results of raster scanning showed that substrate pit defects could be effectively isolated by using suture layers.

The laser-induced damage of thermal–mechanical failure at 1064 nm was induced primarily by localized electronic field

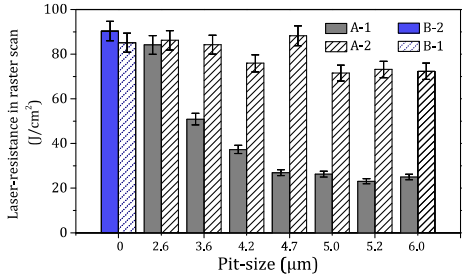

Fig. 5. Laser resistance in raster scanning mode of A-1, A-2, B-1, and B-2 samples.

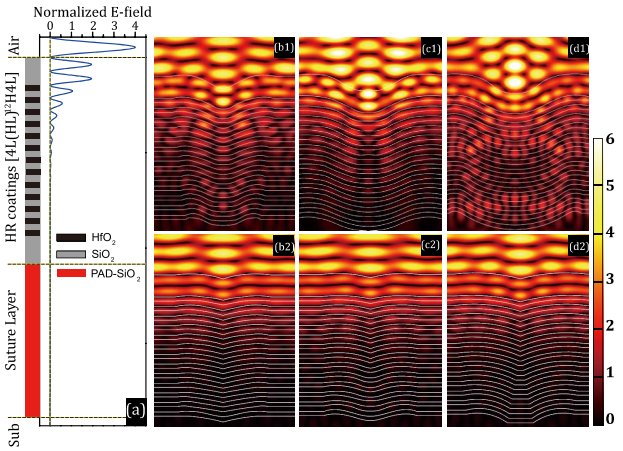

Fig. 6. Normalized e-field distribution calculated in (a) B-1 and B-2, and likewise with A-1 having coated pit sizes of (c) 2.6 μm, (d) 4.2 μm, and (e) 6.0 μm, and A-2 with pit sizes of (f) 2.6 μm, (g) 4.2 μm, and (h) 6.0 μm.

(e-field) enhancement [23,24]. We investigated the dependence of the e-field enhancement on the pit size. The e-field distributions on the pitted sites were simulated using the finite element method, over a rectangular and 2D simulation domain. For the e-field simulation, to obtain accurate results, the rectangular simulation domain was gridded with sufficiently small spaces to ensure that there were at least 10 meshes per wavelength. Furthermore, periodic boundary conditions were applied in the x-direction, and perfectly matched layer boundary conditions were applied in the y-direction. The simulation was performed using a 1064 nm plane wave as the incident field, as shown in Fig. 6. For the undeformed coating samples (B-1 and B-2), their e-field distribution has a topical feature nearly coincident, as shown in Fig. 6(a). The position of the highest e-field value in these coatings lies in the surface layers, namely, the overcoat and the first HfO_2/SiO_2 deposition period. The surface layers are easily damaged when the e-field distribution severely deviates from the designed ones, because it suffers the most laser fluence deposition during laser irradiation. The deformational coating changes the e-field distribution, and the laser resistances of the coatings are inversely proportional to the e-field enhancement. For samples A-1 and A-2, we extracted the reflective index profiles by image processing with SEM-FIB figures and calculated the actual e-field distribution, as shown in Fig. 5. For A-1, the deformed functional layer could be equivalent to a microscale concave mirror, where the light was focalized on the axes along the groove bottom. The light intensification occurred in the coating surface, especially at the air/coating interface, whose e-field intensity was designed as 0. However, for A-2, the light intensification was not as obvious as A-1 because the suture layer relieved the geometrical deformation in the functional layers. Though the deformation did not completely vanish, the suture layer could lower the probability of damage induced by e-field intensification.

In conclusion, a suture layer formed using PIAD was introduced into HR coating deposition to isolate the impact of substrate pit defects. The suture layer also effectively controlled the global stress in instances of coating cracking failures. The cross section results determined by SEM-FIB demonstrated internal crack elimination. The laser resistance of the pitted region was not related to the pit size. The numerical calculation of e-field distribution showed that a suture layer effectively decreases the e-field value of the surface layer of HR coatings. Though the laser resistance was partly influenced by nodule defects introduced by the PIAD process, coating techniques involving suture layers is still a promising way to improve the laser damage performance of surfaces, especially for substrates having low surface quality. The suturing layer could be used for smoothing the substrate pit geometrically and lower the probability of damage induced by e-field intensification.

Funding. National Natural Science Foundation of China (NSFC) (61405225, 61505227, 61308021); Youth Innovation Promotion Association of the Chinese Academy of Sciences (CAS).

Acknowledgment. The authors would like to express their gratitude to Prof. Zhengxiu Fan. The authors would like to acknowledge Dawei Li for assistance with LIDT testing, and Zhengyuan Bai and Qisong Li for assistance with the substrate preparation.

REFERENCES

1. C. J. Stolz, Philos. Trans. R. Soc. A **370**, 4115 (2012).
2. D. Besnard, Eur. Phys. J. D **44**, 207 (2007).
3. D. Hu, J. Dong, D. Xu, X. Huang, W. Zhou, X. Tian, D. Zhou, H. Guo, W. Zhong, X. Deng, Q. Zhu, and W. Zheng, Chin. Opt. Lett. **13**, 041406 (2015).
4. Z. W. Zhu, F. Shi, X. G. Cheng, C. Shen, W. Wan, and Y. Tian, Chin. Opt. Lett. **13**, 052401 (2015).
5. J. Neauport, L. Lamaignere, H. Bercegol, F. Pilon, and J. C. Birolleau, Opt. Express **13**, 10163 (2005).
6. J. Yoshiyama, F. Y. Genin, A. Salleo, I. Thomas, M. R. Kozlowski, L. M. Sheehan, I. D. Hutcheon, and D. W. Camp, Proc. SPIE **2744**, 220 (1997).
7. P. E. Miller, J. D. Bude, T. I. Suratwala, N. Shen, T. A. Laurence, W. A. Steele, J. Menapace, M. D. Feit, and L. L. Wong, Opt. Lett. **35**, 2702 (2010).
8. C. J. Stolz, M. D. Feit, and T. V. Pistor, Appl. Opt. **45**, 1594 (2006).
9. X. Cheng, A. Tuniyazi, J. Zhang, T. Ding, H. Jiao, B. Ma, Z. Wei, H. Li, and Z. Wang, Appl. Opt. **53**, A62 (2014).
10. R. J. Tench, R. Chow, and M. R. Kozlowski, Proc. SPIE **2114**, 415 (1994).
11. S. R. Qiu, J. E. Wolfe, A. Monterrosa, W. A. Steele, N. E. Teslich, M. D. Feit, T. V. Pistor, and C. J. Stolz, Proc. SPIE **7842**, 78421X (2010).
12. Y. Chai, M. Zhu, Z. Bai, K. Yi, H. Wang, Y. Cui, and J. Shao, Opt. Lett. **40**, 1330 (2015).
13. Y. Chai, M. Zhu, H. Wang, H. Xing, Y. Cui, J. Sun, K. Yi, and J. Shao, Sci. Rep. **6**, 27076 (2016).
14. C. J. Stolz, J. E. Wolfe, J. J. Adams, M. G. Menor, N. E. Teslich, P. B. Mirkari, J. A. Folta, R. Soufli, C. S. Menoni, and D. Patel, Appl. Opt. **53**, A291 (2014).
15. Y. Chai, M. Zhu, K. Yi, H. Qi, H. Wang, W. Sun, Z. Yu, Z. Bai, Y. Zhao, and J. Shao, Proc. SPIE **9237**, 92370 (2014).
16. Y. Chai, M. Zhu, K. Yi, W. Zhang, H. Wang, Z. Fang, Z. Bai, Y. Cui, and J. Shao, Opt. Lett. **40**, 3731 (2015).
17. R. Thielsch, A. Gatto, and N. Kaiser, Appl. Opt. **41**, 3211 (2002).
18. H. Xing, M. Zhu, Y. Chai, K. Yi, J. Sun, Y. Cui, and J. Shao, Opt. Lett. **41**, 1253 (2016).
19. W. Liu, C. Wei, K. Yi, and J. Shao, Chin. Opt. Lett. **13**, 041407 (2015).
20. J. Liu, W. Zhang, H. Cui, J. Sun, H. Li, K. Yi, and M. Zhu, Chin. Opt. Lett. **12**, 083101 (2014).
21. X. Liu, Y. Zhao, Y. Gao, D. Li, G. Hu, M. Zhu, Z. Fan, and J. Shao, Appl. Opt. **52**, 2194 (2013).
22. S. Kimura and C. Munakata, Appl. Opt. **27**, 84 (1988).
23. C. J. Stolz, M. D. Feit, and T. V. Pistor, Appl. Opt. **47**, C162 (2008).
24. X. Cheng, J. Zhang, T. Ding, Z. Wei, H. Li, and Z. Wang, Light Sci. Appl. **2**, e80 (2013).